Manuscript submitted to
AIMS' Journals
Volume **X**, Number **0X**, XX **200X**

doi:10.3934/xx.xx.xx.xx

pp. **X–XX**

A KINETIC THEORY DESCRIPTION OF LIQUID MENISCI AT THE MICROSCALE

Paolo Barbante

Politecnico di Milano, MOX, Dipartimento di Matematica
Piazza Leonardo da Vinci, 32
20133 Milan, Italy

Aldo Frezzotti and Livio Gibelli

Politecnico di Milano, Dipartimento di Scienze e Tecnologie Aerospaziali
Via La Masa 34
20156 Milan, Italy

(Communicated by the associate editor name)

Abstract. A kinetic model for the study of capillary flows in devices with microscale geometry is presented. The model is based on the Enskog-Vlasov kinetic equation and provides a reasonable description of both fluid-fluid and fluid-wall interactions. Numerical solutions are obtained by an extension of the classical Direct Simulation Monte Carlo (DSMC) to dense fluids. The equilibrium properties of liquid menisci between two hydrophilic walls are investigated and the validity of the Laplace-Kelvin equation at the microscale is assessed. The dynamical process which leads to the meniscus breakage is clarified.

1. **Introduction.** Micro electromechanical systems (MEMS) have found an increased application in a variety of industrial and medical fields [24]. Their reliability is often limited by phenomena of spontaneous adhesion between parts which should maintain the capability of relative motion. The issues of catastrophic adhesion, but also of dangerous increments of friction, are referred to as "stiction", contraction of "static friction" [25]. Although the mechanisms leading to spontaneous adhesion are still under investigation, some tribological models propose an explanation based on the combined actions of surface roughness and intermolecular forces [20]. An especially important role is played by the attractive force due to liquid menisci that typically form between solid surfaces of devices exposed to high humidity conditions. This adhesion mechanism is commonly investigated on the basis of the continuum theory of capillarity [26, 2]. However, the validity of the macroscopic approach is not obvious when applied to physical processes at the micro/nano scale. The need of a deeper understanding of capillary forces contribution to adhesion phenomena has thus triggered a number of studies based on molecular dynamics (MD) simulations [8, 22]. Although MD can provide an adequate description of the liquid and vapor phases, including liquid-vapor and fluid-solid interfaces, it is computationally very expensive.
The aim of the present work is to investigate both the static and dynamic behavior

2010 *Mathematics Subject Classification.* Primary: 82C40, 82C26; Secondary: 82C80.
Key words and phrases. Enskog-Vlasov equation, microchannels, liquid meniscus, surface tension, two-phase flow.

of liquid menisci between two solid surfaces by a mathematical model based on Enskog-Vlasov (EV) kinetic equation [17]. As described in section 2, EV equation provides an approximate description of a fluid composed by atoms interacting by a potential obtained by adding a soft attractive tail to the hard sphere repulsive contribution. A closed kinetic equation for the *one-particle* distribution function is obtained by assuming that the hard sphere contribution can be dealt with by Enskog collision term [10], whereas the soft tail is taken into account by a self-consistent force field, determined by a linear functional of the fluid number density. The simplified physics leading to EV equation has a number of disadvantages which make comparisons with more complex models difficult. It is easily shown that the fluid governed by EV equation obeys a generalized van der Waals equation of state [15]. As a consequence, the liquid-vapor coexistence diagram, referred to critical quantities, is rather different from the corresponding diagram for the Lennard-Jones fluid [19]. Moreover, the fluid transport properties are determined only by the hard sphere potential, since the attractive tail appears in the kinetic equation as an external force, although determined by fluid density [23]. In spite of the simplified treatment of pair correlations in the dense phase [17], EV equation provides a reasonably accurate description of two-phase flows, automatically tracking the formation of vapor-liquid [3, 13, 15] and solid-liquid interfaces [16, 14].
In the case of non-equilibrium flows, the model is able to take into account kinetic regions (Knudsen layers) close to vapor-liquid interfaces. It should also be noted that the evaporation coefficient values obtained from EV equation are quite close to those predicted by MD simulations of Lennard-Jones fluid [15]. The main advantage of using EV kinetic description is associated with the possibility of adopting an extension [12] of Direct Simulation Monte Carlo (DSMC) [5] to approximate its solutions. As explained in section 3, the computational cost of EV equation based DSMC simulations is considerably lower than typical MD simulations with comparable atoms number.
The study of liquid menisci behavior according to the adopted kinetic model has been organized in a number of steps, described in sections 4.1, 4.2, 4.3 and 4.4, respectively. First, the equilibrium properties of an isolated cylindrical droplet are established by computing the surface tension by different methods. The model of fluid-wall interaction described in section 2 is then introduced in section 4.2 to study the dependence of the contact angle on the fluid-wall interaction potential parameters, when a droplet is in equilibrium, in contact with a planar wall. The equilibrium property of a meniscus bridging two planar solid walls are studied in section 4.3 to assess the validity of Kelvin-Laplace equation for small wall spacing. Finally, the spontaneous breakage of a meniscus bridging two planar solid walls is studied by unsteady simulations, described and discussed in section 4.4.

2. **Mathematical formulation.**

We consider a system composed by a monoatomic fluid interacting with solid walls. Fluid molecules have mass m_g and nominal diameter σ_g, whereas m_w and σ_w are the mass and the nominal diameter of wall molecules. Fluid-fluid, $\phi_{gg}(\rho)$, and fluid-wall, $\phi_{gw}(\rho)$, interaction forces are supposed to be given by the following Sutherland potentials

$$\phi_{gg}(\rho) = \begin{cases} +\infty & \rho < \sigma_g \\ \psi_{gg}(\rho) & \rho \geq \sigma_g \end{cases} \qquad \phi_{gw}(\rho) = \begin{cases} +\infty & \rho < \sigma_{gw} \\ \psi_{gw}(\rho) & \rho \geq \sigma_{gw} \end{cases} \tag{1}$$

which depend on the distance $\rho = ||\mathbf{r}_1 - \mathbf{r}||$ between two molecules located at $\mathbf{r}$ and $\mathbf{r}_1$, respectively. As shown above, ϕ_{gg} and ϕ_{gw} are obtained by superposing the soft tails, $\psi_{gg}(\rho)$ and $\psi_{gw}(\rho)$, to the hard sphere potentials determined by the hard sphere diameters σ_g and $\sigma_{gw} = (\sigma_g + \sigma_w)/2$, respectively. If interactions between fluid and wall molecules are momentarily disregarded, the following exact kinetic equation can be obtained for the one-particle distribution function $f(\mathbf{r}, \mathbf{v}|t)$ of fluid molecules [23], namely

$$\frac{\partial f}{\partial t} + \mathbf{v} \cdot \nabla_{\mathbf{r}} f = \frac{1}{m_g} \nabla_{\mathbf{v}} \cdot \left\{ \int_{-\infty}^{\infty} d\mathbf{v}_1 \int_{\rho > \sigma_g} d\mathbf{r}_1 \frac{d\phi_{gg}}{d\rho} f_2(\mathbf{r}, \mathbf{v}, \mathbf{r}_1, \mathbf{v}_1|t) \hat{\mathbf{k}} \right\} +$$

$$\sigma_g^2 \int_{-\infty}^{\infty} d\mathbf{v}_1 \int_{\mathcal{S}_+} d^2\hat{\mathbf{k}} \left\{ f_2(\mathbf{r}, \mathbf{v}^*, \mathbf{r} + \sigma_g \hat{\mathbf{k}}, \mathbf{v}_1^*|t) - f_2(\mathbf{r}, \mathbf{v}, \mathbf{r} - \sigma_g \hat{\mathbf{k}}, \mathbf{v}_1|t) \right\} (\mathbf{v}_r \cdot \hat{\mathbf{k}}) \quad (2)$$

Eq. (2) is not closed because it includes the two particle distribution function $f_2(\mathbf{r}, \mathbf{v}, \mathbf{r}_1, \mathbf{v}_1|t)$ which appears in the two integrals at its *r.h.s.*. The first one takes into account long range, usually attractive, interactions. More intense short range interactions, caused by repulsive forces, are taken into account by the second integral as binary hard sphere collisions. These are determined by the relationships

$$\mathbf{v}^* = \mathbf{v} + \left(\mathbf{v}_r \cdot \hat{\mathbf{k}} \right) \hat{\mathbf{k}} \quad (3)$$

$$\mathbf{v}_1^* = \mathbf{v}_1 - \left(\mathbf{v}_r \cdot \hat{\mathbf{k}} \right) \hat{\mathbf{k}} \quad (4)$$

being $\mathbf{v}_r = \mathbf{v}_1 - \mathbf{v}$ the relative velocity of two colliding molecules, $\hat{\mathbf{k}}$ a unit vector which assigns the relative position of two molecules at the time of their impact, whereas $(\mathbf{v}^*, \mathbf{v}_1^*)$ are pre-collision velocities. The following closed kinetic equation:

$$\frac{\partial f}{\partial t} + \mathbf{v} \cdot \nabla_{\mathbf{r}} f + \frac{\mathbf{F}_{gg}(\mathbf{r}|t)}{m_g} \cdot \nabla_{\mathbf{v}} f = C_{gg}(f, f), \quad (5)$$

called Enskog-Vlasov equation [17, 23], can be derived by the assumptions listed below:

1. Correlations between molecules are neglected in the first integral on the r.h.s. of Eq. (2), i.e. $f_2(\mathbf{r}, \mathbf{v}, \mathbf{r}_1, \mathbf{v}_1|t) = f(\mathbf{r}, \mathbf{v}|t) f(\mathbf{r}_1, \mathbf{v}_1|t)$.
2. In the second integral on the r.h.s. of Eq. (2), the two particle distribution function f_2 is written as in the Enskog theory of dense gases[10]:

$$f_2(\mathbf{r}, \mathbf{v}, \mathbf{r} - \sigma_g \hat{\mathbf{k}}, \mathbf{v}_1|t) = \chi_{gg}(\mathbf{r}, \mathbf{r} - \sigma_g \hat{\mathbf{k}}|n) f(\mathbf{r}, \mathbf{v}|t) f(\mathbf{r} - \sigma_g \hat{\mathbf{k}}, \mathbf{v}_1|t) \quad (6)$$

where χ_{gg} is the contact value of the pair correlation function of a hard sphere fluid in equilibrium.

The self-consistent force field $\mathbf{F}_{gg}(\mathbf{r}|t)$, generated by the tail potential, and the hard sphere collision integral $C_{gg}(f, f)$ are given by the following expressions:

$$\mathbf{F}_{gg}(\mathbf{r}|t) = \int_{\rho > \sigma_g} \frac{d\phi_{gg}}{d\rho} \frac{\mathbf{r}_1 - \mathbf{r}}{\|\mathbf{r}_1 - \mathbf{r}\|} n(\mathbf{r}_1|t) \, d\mathbf{r}_1 \quad (7)$$

$$C_{gg}(f, f) = \sigma_g^2 \int_{\mathcal{S}_+} \left\{ \chi_{gg}(\mathbf{r}, \mathbf{r} + \sigma_g \hat{\mathbf{k}}) f(\mathbf{r} + \sigma_g \hat{\mathbf{k}}, \mathbf{v}_1^*|t) f(\mathbf{r}, \mathbf{v}^*|t) - \right.$$

$$\left. \chi_{gg}(\mathbf{r}, \mathbf{r} - \sigma_g \hat{\mathbf{k}}) f(\mathbf{r} - \sigma_g \hat{\mathbf{k}}, \mathbf{v}_1|t) f(\mathbf{r}, \mathbf{v}|t) \right\} (\mathbf{v}_r \cdot \hat{\mathbf{k}})^+ d\mathbf{v}_1 d^2\hat{\mathbf{k}} \quad (8)$$

When describing a fluid at the scale of molecular size, as EV equation does, dealing with fluid solid interaction by the same formalism used in rarefied gas dynamics[7]

would represent a too drastic simplification. Fortunately, the same arguments leading to Eq. (5) allow formulating a fluid-solid interaction model with similar structure [14]. As above, the soft tail of the fluid-solid interaction potential $\phi_{gw}(\rho)$ is assumed to give rise to the force field $\mathbf{F}_{gw}(\mathbf{r})$, determined by the given number density $n_w(\mathbf{r}_1)$ of the solid as:

$$\mathbf{F}_{gw}(\mathbf{r}) = \int_{\rho>\sigma_{gw}} \frac{d\phi_{gw}}{d\rho} \frac{\mathbf{r}_1 - \mathbf{r}}{\|\mathbf{r}_1 - \mathbf{r}\|} n_w(\mathbf{r}_1)\, d\mathbf{r}_1 \tag{9}$$

The short range repulsive forces felt by a fluid molecule close to the solid lattice is, as above, described by a sequence of binary hard sphere collisions through the collision integral:

$$C_{gw}(f_w, f) = \sigma_{gw}^2 \int_{\mathcal{S}_+} \Big\{ \chi_{gw}(\mathbf{r}, \mathbf{r} + \sigma_{gw}\hat{\mathbf{k}}) f_w(\mathbf{r} + \sigma_{gw}\hat{\mathbf{k}}, \mathbf{v}_1^*|t) f(\mathbf{r}, \mathbf{v}^*|t) - \chi_{gw}(\mathbf{r}, \mathbf{r} - \sigma_{gw}\hat{\mathbf{k}}) f_w(\mathbf{r} - \sigma_{gw}\hat{\mathbf{k}}, \mathbf{v}_1|t) f(\mathbf{r}, \mathbf{v}|t) \Big\} (\mathbf{v}_r \cdot \hat{\mathbf{k}})^+ d\mathbf{v}_1 d^2\hat{\mathbf{k}} \tag{10}$$

being f_w is the distribution function of wall molecules.
The two new terms defined by Eqs. (9,10) add to the corresponding ones in Eq. (5) to give:

$$\frac{\partial f}{\partial t} + \mathbf{v} \cdot \nabla_{\mathbf{r}} f + \frac{\mathbf{F}(\mathbf{r}|t)}{m_g} \cdot \nabla_{\mathbf{v}} f = C_{gg}(f, f) + C_{gw}(f, f) \tag{11}$$

being $\mathbf{F}(\mathbf{r}|t) = \mathbf{F}_{gg}(\mathbf{r}|t) + \mathbf{F}_{gw}(\mathbf{r})$ the total field. In absence of long range spatial correlations, $\mathbf{F}_{gg}(\mathbf{r}|t)$ and $\mathbf{F}_{gw}(\mathbf{r})$ are linear functionals of the fluid number density $n(\mathbf{r}|t)$ and wall number density $n_w(\mathbf{r})$, respectively. The model physical properties are defined by the interaction potentials, the pair correlation functions χ_{gg} and χ_{gw} and f_w. No explicit assumption is made about the interaction among wall molecules and it is simply assumed that walls are in a prescribed state of equilibrium which is not altered by the interaction with the fluid. Hence, the velocity distribution function f_w will take the following form

$$f_w(\mathbf{r}, \mathbf{v}) = \frac{n_w(\mathbf{r})}{[2\pi R_w T_w(\mathbf{r})]^{3/2}} \exp\left\{ -\frac{[\mathbf{v} - \mathbf{u}_w(\mathbf{r})]^2}{2R_w T_w(\mathbf{r})} \right\} \tag{12}$$

being $n_w(\mathbf{r})$, $T_w(\mathbf{r})$ and $\mathbf{u}_w(\mathbf{r})$ the *prescribed* wall molecules number density, temperature and mean velocity, respectively. The gas constant R_w is defined as k_B/m_w, where k_B is the Boltzmann constant.

According to the revised Enskog theory (RET) [27], the fluid-fluid correlation function, χ_{gg}, is a functional of the density field $n(\mathbf{r}|t)$ and, although an expression can be obtained as a cluster expansion of the density, for practical applications simpler expressions are needed. As suggested in Ref. [11], the contact value of the pair correlation function is locally taken as that of a homogeneous fluid in equilibrium at density $\bar{n}$, defined as the average density over a sphere of diameter σ_g centered at the point of contact of the colliding fluid molecules. The specific form of $\chi_{gg}(\bar{n})$ is taken from an approximate expression for the contact value of the pair correlation function of a single component hard sphere gas in uniform equilibrium [6], namely

$$\chi_{gg}(\bar{n}) = \frac{1}{2} \frac{2 - \tilde{\eta}_g}{(1 - \tilde{\eta}_g)^3}, \qquad \tilde{\eta}_g = \frac{\pi}{6} \bar{n} \sigma_g^3 \tag{13}$$

Eq. (13) provides a very accurate approximation of the contact value of the uniform equilibrium pair correlation function in a single component hard sphere gas. The

calculation of the fluid-wall pair correlation function, χ_{gw}, is more problematic. For the sake of simplicity, it has been assumed that excluded volume effects are determined solely by wall molecules through a modified number density $\tilde{n}_w$. This number density can be different from the value of n_w that appears in Eq. (9). The rationale is to be able to tune independently the behavior of the long range attractive interaction and of the short range repulsive interaction between fluid and wall. The specific form of $\chi_{gw}(\tilde{n}_w)$ is given by Eq. (13), with $\tilde{\eta}_g$ replaced by $\tilde{\eta}_w = \pi\tilde{n}_w\sigma_{gw}^3/6$. Although the use of Eq. (13) in the present context is questionable, the physical consequences of the above assumptions are quite reasonable. Actually, it is easily shown that, in the presence of a wall density gradient, the hard sphere term produces a net repulsive force. The rate of change of momentum associated to short range gas-wall collisions is

$$\mathbf{F}^{(coll)}(\mathbf{r}) = m_g \int \mathbf{v} C_{gw}(f_w, f)\, d\mathbf{v} \tag{14}$$

The above expression can be used to obtain the collisional force on a test gas atom at rest in the vicinity of the surface of a homogeneous wall which occupies the half space $y_1 < 0$, y_1 being the space coordinate normal to the wall. Accordingly, it is assumed that the solid density $n_w(\mathbf{r}_1)$ is given by the step function:

$$n_w(y_1) = \begin{cases} n_w & y_1 \le 0 \\ 0 & y_1 > 0 \end{cases} \tag{15}$$

The temperature T_w of the wall is taken uniform and constant. Substitution of the Dirac's δ-function $\delta(\mathbf{v})$ into Eq. (14) in place of $f(\mathbf{v})$ and elementary manipulations lead to the result that $\mathbf{F}^{(coll)}(\mathbf{r})$ is normal to the wall surface and depends only on the y component of the test atom position. The y component of the collisional force, $F_y^{(coll)}$, has the following simple expression

$$F_y^{(coll)}(y) = \begin{cases} \pi\sigma_{gw}^2 \dfrac{m_g}{m_g + m_w} n_w \chi_{gw}(\tilde{n}_w) k_B T_w \left[1 - \left(\dfrac{y}{\sigma_{gw}}\right)^2\right] & |y| \le \sigma_{gw} \\ 0 & |y| > \sigma_{gw} \end{cases} \tag{16}$$

Eq. (16) shows that $F_y^{(coll)}$ is different from zero where the protection sphere of center $\mathbf{r}$ and radius σ_{gw} partially overlaps to the wall and it is unevenly exposed to collisions. It is to be noted that $\mathbf{F}_{(coll)}$ is essentially related to the non-local structure of Enskog's collision term, in which collision partners occupy positions one atomic diameter apart. Such repulsive force would vanish if $\mathcal{C}_{gw}(f_w, f)$ were replaced with a local Boltzmann-like collision term. The amplitude of $F_y^{(coll)}$ is proportional to $\chi_{gw}(\tilde{n}_w)$, which appears to be a key quantity to control the repulsive intensity of short range gas-wall interaction. For typical values of solid phase density, in the presence of a steep wall density gradient, the hard sphere term produces a net repulsive force strong enough to confine the fluid [14]. Moreover, the behavior of the accommodation coefficients provided by the proposed fluid-wall interaction model are in good agreement with the predictions of molecular dynamics simulations [16].

It is worth stressing that, in the framework of the present model, fluid-wall interaction is not present in the form of a boundary condition, but it is taken into account through explicit, although approximate, interaction terms in the kinetic equation. In particular, it is assumed that the motion of a gas molecule in the vicinity of the wall is determined by the stationary force field $\mathbf{F}_{gw}(\mathbf{r})$ generated by the long range potential tails of wall molecules, when the distance ρ exceeds σ_{gw}.

Fluctuations of $\mathbf{F}_{gw}(\mathbf{r})$ due to the random motions of wall molecules are neglected. At shorter distances, the effect of intense repulsive forces is accounted for by the collision integral $C_{gw}(f_w, f)$ which describes binary elastic collisions between gas and wall molecules. It is therefore assumed that repulsion on a gas molecule is caused just by the closest wall molecule. However, the collective effect of nearby wall molecules on the frequency of binary encounters is felt through χ_{gw}.

3. **Numerical method.** The complex mathematical structure of the hard sphere collision integrals C_{gg}, Eq. (8) and C_{gw}, Eq. (10), requires the numerical treatment of Eq. (11), which can be efficiently solved by an extension of the classical direct simulation Monte Carlo (DSMC) particle scheme to dense fluids [12]. The distribution function f of the fluid is represented by N_p computational particles each one characterized by its position $\mathbf{r}_i$ and velocity $\mathbf{v}_i$. The spatial domain is divided into a suitable number of cells. In the simulation of a two-dimensional flow-field, the number of computational particles, N_p, can always be made equal to the number of real molecules by a proper choice of the height L_z of the computational domain along the homogeneity direction z. In three-dimensional or axisymmetric simulations such a choice is not possible and therefore a weight has to be introduced, equal to the ratio of the number of real to the number of simulation particles. In that way, N_p is no more equal to the real number of particles present in the physical domain and the weight can be seen as the inverse of the number of similar real systems that are simulated to obtain good statistics.

The solution of Eq. (11) is performed by a time splitting procedure in which the distribution function, represented by the computational particles, is advanced from time t to time $t + \Delta t$ in three stages, according to the following scheme:

$$f(t) \xrightarrow[1]{Free\ flight} f^{(1)}(t+\Delta t) \xrightarrow[2]{Wall\ coll.} f^{(2)}(t+\Delta t) \xrightarrow[3]{Gas\ coll.} f(t+\Delta t) \tag{17}$$

In the first free flight stage, collisions are neglected and the distribution function is advanced from its initial value $f(\mathbf{r}, \mathbf{v}|t)$ to a provisional value $f^{(1)}(\mathbf{r}, \mathbf{v}, |t + \Delta t)$ solving the equation

$$\frac{\partial f}{\partial t} + \mathbf{v} \cdot \nabla_{\mathbf{r}} f + \frac{\mathbf{F}(\mathbf{r}|t)}{m_g} \cdot \nabla_{\mathbf{v}} f = 0 \tag{18}$$

In practice this is accomplished by updating positions and velocities of fluid particles according to

$$\mathbf{r}_i(t+\Delta t) = \mathbf{r}_i(t) + \mathbf{v}_i(t)\Delta t + \frac{\mathbf{F}[\mathbf{r}_i(t)|t]}{m_g}\frac{(\Delta t)^2}{2} \tag{19}$$

$$\mathbf{v}_i(t+\Delta t) = \mathbf{v}_i(t) + \frac{\mathbf{F}[\mathbf{r}_i(t)|t]}{m_g}\Delta t \tag{20}$$

In the second and third stages, fluid-wall and fluid-fluid short range interactions are considered respectively. The distribution function is updated as

$$f^{(2)}(\mathbf{r}, \mathbf{v}|t+\Delta t) = f^{(1)}(\mathbf{r}, \mathbf{v}|t+\Delta t) + C_{gw}(f_w, f^{(1)})\Delta t \tag{21}$$

$$f(\mathbf{r}, \mathbf{v}|t+\Delta t) = f^{(2)}(\mathbf{r}, \mathbf{v}|t+\Delta t) + C_{gg}(f^{(2)}, f^{(2)})\Delta t \tag{22}$$

Particle positions are not changed in these two stages, but their velocity $\mathbf{v}_i$ changes according to stochastic rules consistent with the mathematical structure of the collision integrals $C_{gw}(f_w, f)$ and $C_{gg}(f, f)$ [12]. The overall time splitting scheme is first order accurate in time step Δt and in cell size $\Delta r = \Delta x = \Delta y$. An acceptable

level of accuracy is guaranteed in all the phases of the time splitting procedure if Δt and Δr fulfill the conditions

$$\Delta t < \min(\tau_{gg}, \tau_{gw}) \tag{23}$$

$$\Delta r < \min(\lambda_{gg}, \lambda_{gw}) \tag{24}$$

τ_{gg}, τ_{gw} are the mean free times between collisions dictated by fluid-fluid and fluid-wall short range interactions and $\lambda_{gg}, \lambda_{gw}$ are the respective mean free paths. Unless the fluid is dense everywhere in the computational domain, τ_{gw} can be much smaller than τ_{gg}. In this case condition given by Eq. (23) would restrict the time step to a value that is adequate in a layer of thickness σ_{gw} close to the wall, but unnecessarily small in the rest of the domain. A straightforward modification of the time splitting procedure is introduced to overcome such a limitation. Fluid particles that are likely to collide with the wall in the time interval $(t, t+\Delta t)$ are identified. For these particles the first and second stage are computed as a sequence of sub cycles each with a time step of the order τ_{gw}, the number of sub cycles being $\mathcal{N}_s \approx \Delta t/\tau_{gw}$. A main point of the numerical code is the computation of the self-consistent force field, $\mathbf{F}(\mathbf{r}|t)$. In the two-dimensional cases considered in the following, the integration over the homogeneity direction z_1 is first carried out with a generalized Romberg method, thus reducing Eq. (7) to

$$\mathbf{F}(x, y|t) = \int [(x_1 - x)\mathbf{i} + (y_1 - y)\mathbf{j}]\, n(x_1, y_1|t)\mathcal{K}(x_1 - x, y_1 - y)\, dx_1 dy_1 \tag{25}$$

where the component of the force field along the z axis is equal to zero. The remaining two-dimensional integral is performed by a simple mid-point quadrature formula. It is worth noticing that in Eq. (25) the kernel $\mathcal{K}(x_1 - x, y_1 - y)$ depends on the chosen potential but not on the actual value of the density field. This fact makes possible to compute the kernel $\mathcal{K}$ only once for a suitable range of the variables $x_1 - x$ and $y_1 - y$. As a matter of fact, in principle, each particle feels the force field generated by all the particles in the domain. Hence, if N_c is the total number of computational cells, the computation of the force field would have a cost of the order of N_c^2. In practice, to reduce the problem to a feasible size, we introduce a cut-off distance and include in the computation of the force field only the contribution of the cells inside the cut-off region. A comparison of the computational performances of the DSMC scheme described above with those of similar MD simulations is in order, before describing applications.

First of all, it should be noted that the computational effort of each of the three stages composing the DSMC scheme is proportional to the simulation particles number N_p. A similar dependence on N_p holds for MD simulations adopting potential range cut-off and some form of nearest neighbor indexing [1]. For the applications described in this paper, the time step and simulation duration would also be very close. However, the DSMC computational cost per particle is generally smaller. Atoms collisional interaction (stage 2) is treated stochastically, the easily estimated number of collisions to be computed at each time step being much smaller than N_p. The calculation of the self-consistent force field is, in principle, very similar to the way MD computes forces. However, the DSMC computational effort is proportional to the product of the spatial cell number times the number of spatial cells within the cut-off distance. Both factors are much smaller that the number of simulation atoms. Moreover, the elements of the discretized kernel $\mathcal{K}$, see Eq. (25), are computed once and stored in a small matrix, thus reducing the forces calculation to vector-matrix multiplications. Nevertheless, it should be observed that the

impact of the force field calculation on the overall DSMC performances depends on the dimensionality of the problem. DSMC-MD comparisons of spatially one-dimensional flow simulations show that DSMC runs about $50-60$ times faster than a similar MD simulation with the same atoms number. In the present work, where two-dimensional planar simulations are considered, the typical particles number is around 7.5×10^5. Computing time to perform 10^5 time steps amount to about 20 hours on a single quadcore processor running at $2.9GHz$. *OpenMP* directives have been used to split the particles advection and force field calculation steps among three cores, obtaining a speed up of two over the sequential algorithm version. The cylindrical droplet simulations described in Sec. 4.1 have been performed with 2.52 millions particles. In this case, the computing time is around 60 hours on the same equipment. Comparisons with similar MD simulations show that, in these cases, DSMC runs about 10 times faster than MD. The considerations presented above suggest that the computational advantages of DSMC simulations, based on EV model, are limited to two-dimensional planar and axisymmetric flow geometries [4], being strongly reduced for fully three-dimensional flow geometry.

4. **Static and dynamic properties of liquid menisci.** In the present work, the fluid-fluid and fluid-wall long range interactions, Eqs. (1), are supposed to be given by soft-attractive algebraic and exponential potential tails, respectively, that is

$$\psi_{gg}(\rho) = -\overline{\phi}_{gg}\left(\frac{\rho}{\sigma_g}\right)^{-\gamma_{gg}} \tag{26}$$

$$\psi_{gw}(\rho) = -\overline{\phi}_{gw}\exp\left[-\frac{(\rho-\sigma_{gw})}{\gamma_{gw}}\right] \tag{27}$$

where $\overline{\phi}_{gg}$, $\overline{\phi}_{gw}$ are the depths of the potential wells and γ_{gg}, γ_{gw} tune the potential ranges. In all the computations shown below γ_{gg} has been set equal to 6 in order to match the attractive tail of the Lennard-Jones potential. Unless otherwise specified, the remaining model parameters have been set as follows: $\overline{\phi}_{gg}/k_BT_0=1.0$, $\sigma_w/\sigma_g=1.0$, $m_w/m_g=2$, $n_w\pi\sigma_{gw}^3/6=0.7$, the wall temperature T_w is assumed equal to the fluid temperature. The numerical values assigned to $\tilde{n}_w\pi\sigma_{gw}^3/6$ and λ_{gw} will be discussed in Sec. 4.2. In a typical computation the smallest spatial grid size has been set equal to $0.1\sigma_g$ to resolve the structure of interfaces. The average number of particles per cell has been set approximately equal to 10. The local value is much higher in regions occupied by the liquid phase and lower in the vapor phase. However, the significant spatial scale in the vapor is the mean free path and the number of particles per cubic mean free path has always been above the threshold required by DSMC accuracy. The time step in reduced units has been typically set equal to 0.005. Because of the unsteady character of the flows, macroscopic quantities "snapshots" have been obtained by averaging microscopic particle states over successive time intervals of 200 reduced time units. The cut-off distance for the force-field computation has been set equal to $4\sigma_g$.

4.1. **Evaluation of surface tension.** Surface tension is a key property whose calculation is needed for a proper and adequate description of multi-phase flows. The vapor-liquid interfacial tension of fluid described by the Enskog-Vlasov equation, Eq. (11), has been computed by using two different methods. The first method is based on the microscopic mechanical definition of the surface tension which involves the tensional components of the pressure tensor in an inhomogeneous system.

The second method provides an indirect estimation of the surface tension from the Laplace equation applied to two dimensional cylindrical drops.

From the mechanical standpoint, the surface tension is given by the integrated imbalance of normal and tangential pressure tensor components near the interface under isothermal condition [21]. More specifically, in the case of a planar interface perpendicular to the z-axis, the surface tension is given by

$$\gamma = \int_{-\infty}^{+\infty} dz \, \left[p_0 - p_{xx}(z) \right], \tag{28}$$

where p_0 is the uniform normal pressure which acts on both liquid and vapor phases and p_{xx} is the xx-component of the stress tensor. For a fluid described by the Enskog-Vlasov equation, Eq. (11), the xx-component of the stress tensor is defined as follows

$$\begin{aligned} p_{xx} = nkT - \frac{1}{2}\gamma_{gg}\overline{\phi}_{gg}{\sigma_g}^{\gamma} \int_0^1 d\alpha \int_{||\mathbf{s}||\geq\sigma_g} d\mathbf{s} \, \frac{s_z^2}{||\mathbf{s}||^{\gamma+2}} n\left(z - \alpha s_z\right) n\left(z + s_z - \alpha s_z\right) \\ + {\sigma_g}^3 kT \int_0^1 d\alpha \int_{\mathcal{S}_+} d\mathbf{k} \, k_z^2 \, n\left(z - \alpha\sigma_g k_z\right) n\left(z + \sigma_g k_z - \alpha\sigma_g k_z\right) \\ \chi_{gg}\left[n\left(z - \alpha\sigma_g k_z + \frac{\sigma_g}{2} k_z \right) \right] \end{aligned} \tag{29}$$

The first term on the right hand side of Eq. (29) equals the familiar expression for the pressure in an ideal gas. The second and third terms are due to the long-range attractive and short-range repulsive pair interactions between particles, respectively. In the present work, the surface tension has been computed by numerically solving the spatially one-dimensional form of Eq. (11) through the particle scheme described in Section 3, for a fluid temperature T/T_c varying in the range $[0.66, 0.93]$. T_c is the critical temperature of the hard sphere dense fluid [15]. The spatial domain is a finite symmetric interval $[-L/2, L/2]$ of the z axis and periodic boundary conditions have been assumed at $z = \pm L/2$. Each computation is started by arranging a homogeneous liquid slab at temperature T in the center of the computational domain bounded by two symmetrical empty regions. The thickness of the slab is smaller than L and much wider than the thickness of the vapor-liquid interface to be formed during the simulation. The system evolution is then computed until the evaporation of a part of the liquid brings the liquid and vapor in equilibrium. The system is thermostatted to keep its temperature constant during the transient evaporation phase. For illustrative purposes, in Fig. 1 we report $p_0 - p_{xx}(z)$, whose integral gives the surface tension according to Eq. (28), for different temperature ratio T/T_c. For all the results, the origin has been chosen so that $z/\sigma_g = 0$ corresponds to the equimolar dividing surfaces [21]. The values of the normal and tangential components of the stress tensor are equal in the two coexisting phases which is an indication of phase equilibrium whereas they differ within the interfacial region. As expected, the higher the temperature of the system the smaller is the stress anisotropy. The estimated values of surface tension is reported in the first column of Table 1.

An approximate estimate of the surface tension can be obtained by expanding Eq. (29) with respect to density and its derivatives, so as to transform nonlocal

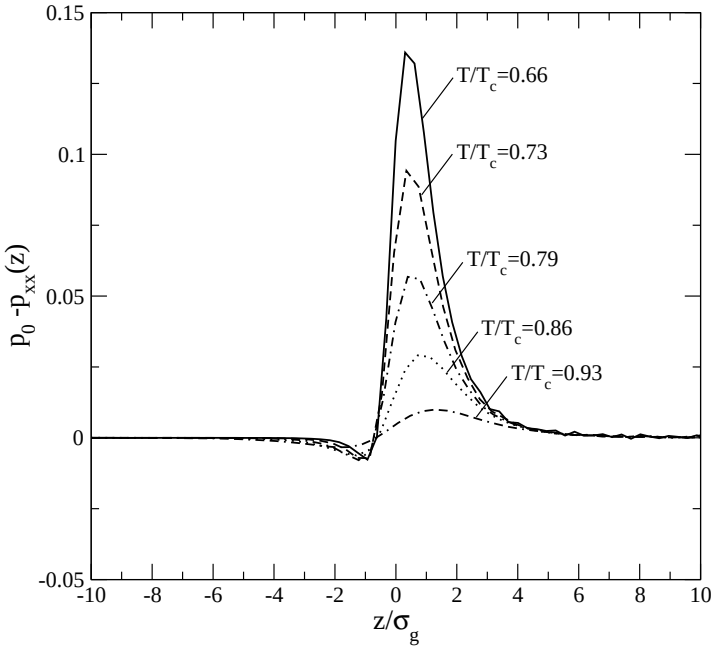

FIGURE 1. Imbalance of normal and tangential pressure tensor components, $p_0 - p_{xx}(z)$, with respect to the direction normal to the interface, z/d, for different temperature, T/T_c.

expressions into local ones. Taking into account terms containing up to second-order spatial derivatives of density, Eq. (29) simplifies to

$$p_{xx} = p_{eq}(n,T) + \alpha(n,T)\left(\frac{dn}{dz}\right)^2 + \beta(n,T)\left(\frac{d^2n}{dz^2}\right) \tag{30}$$

where $p_{eq}(n,T)$, $\alpha(n,T)$ and $\beta(n,T)$ are given by

$$p_{eq}(n,T) = nkT\left[1 + \frac{2}{3}\pi\sigma_g^3 n\chi_{gg}\right] - \frac{2}{3}\pi\sigma_g^3\frac{\gamma_{gg}}{\gamma_{gg}-3}\overline{\phi}_{gg}n^2 \tag{31}$$

$$\alpha(n,T) = \frac{\pi}{45}\sigma_g^5\frac{\gamma_{gg}}{\gamma_{gg}-5}\overline{\phi}_{gg} + \frac{\pi}{45}\sigma_g^5 kT\left(\frac{n^2}{4}\frac{d^2\chi_{gg}}{dn^2} + n\frac{d\chi_{gg}}{dn} - \chi_{gg}\right) \tag{32}$$

$$\beta(n,T) = n\left[\frac{\pi}{45}\sigma_g^5 kTn\left(\frac{n}{4}\frac{d\chi_{gg}}{dn} + 2\chi_{gg}\right) - \frac{2}{45}\pi\sigma_g^5\frac{\gamma_{gg}}{\gamma_{gg}-5}\overline{\phi}_{gg}\right] \tag{33}$$

It can be shown that the non-uniform density profile of the fluid in equilibrium at temperature $T < T_c$ obeys the equation

$$kT\frac{dn}{dz} = n(z)F_z(z) + 2\pi{\sigma_g}^2 n(z)kT\int_{-1}^{1} dk_z\, k_z\chi_{gg}\left[n\left(z - \frac{\sigma_g}{2}k_z\right)\right]n(z - \sigma_g k_z) \tag{34}$$

F_z is given by

$$F_z(z) = 2\pi\overline{\phi}_{gg}\left[{\sigma_g}^{\gamma_{gg}}\int_{\rho>\sigma_g}\frac{(z_1 - z)n(z_1)}{\rho^{\gamma_{gg}}}dz_1 + \int_{\rho\le\sigma_g}(z_1 - z)n(z_1)dz_1\right] \tag{35}$$

where $\rho = \|z - z_1\|$ [15]. With the same approximation used to derive Eq. (30), the solution of the integral equation for the equilibrium density profile, Eq. (34), reduces to finding a solution of the second-order differential equation

$$p_{eq}(n,T) + 3\alpha(n,T)\left(\frac{dn}{dz}\right)^2 + 3\beta(n,T)\left(\frac{d^2n}{dz^2}\right) = p_0 \tag{36}$$

with the boundary conditions

$$\lim_{z\to-\infty} n(z) = n_l(T,p_0) \tag{37}$$

$$\lim_{z\to+\infty} n(z) = n_g(T,p_0) \tag{38}$$

$$\lim_{z\to+\infty} \frac{dn}{dz} = 0 \tag{39}$$

where $n_g(T)$ and $n_l(T)$ are the gas and liquid densities which satisfy the conditions $p_{eq}(n_g,T) = p_{eq}(n_l,T) = p_0$ [15]. The computation of the density profile can be simplified by taking the density n as independent variable, which varies monotonically in the interface region. Setting $\tilde{z} = dn/dz$ shows that $d\tilde{z}/dz = \tilde{z}d\tilde{z}/dn$. Substitution into Eq. (36) leads to a first order differential equation for $\tilde{z}(n)$. In general, given a temperature value $T < T_c$, a solution starting from the initial point $(n_g(T), 0)$ will not reach the point $(n_l(T), 0)$ unless a particular value of the equilibrium pressure $p_0(T)$ is selected. The determination of $p_0(T)$ immediately gives the liquid density, $n_l(T)$, and vapor density, $n_g(T)$, as a function of T. If needed, one further integration provides the density profile $n(x)$. By substituting the solution of Eq. (36) into Eq. (30) and, in turn, Eq. (30) into Eq. (28), we obtained the approximated estimate of the surface tension reported in the second column of Table 1. In the considered range of temperature, results differ from the previous estimates from a minimum of about 5% to a maximum of about 30%.

As mentioned, an indirect estimation of the surface tension has been also obtained from the Laplace equation applied to two dimensional cylindrical droplets. The Laplace equation relates the pressure difference between both sides of a droplet surface to the surface tension γ and the two principal radii of curvature of the droplet, R_1, R_2, that is

$$\Delta p = \gamma\left(\frac{1}{R_1} + \frac{1}{R_2}\right) \tag{40}$$

where $\Delta p = p_l - p_g$ with p_l and p_g the pressure in the liquid and the gas region. As a matter of fact, in Eq. (40) γ is weakly dependent on R_1 and R_2. However, if the droplet is large enough compared to the interfacial region, such a dependence can be disregarded and Eq. (40) can be used to predict the surface tension. Furthermore, in this case the values of p_l and p_g may be identified as the bulk pressure in the center of the droplet and far outside the droplet, respectively. In the present work, a liquid droplet surrounded by the vapor has been obtained by solving numerically the spatially two-dimensional form of Eq. (11) by means of the particle scheme described in Section 3. The spatial domain is a sufficiently large quadratic box $[-L/2, L/2] \times [-L/2, L/2]$ with periodic boundary conditions in both directions. Each computation is started with a two-dimensional droplet placed in the center of the computational domain. As before, the system evolution is computed until liquid and vapor reach the equilibrium and a thermostat is employed to keep the temperature of the system constant during the transient evaporation phase. The surface

tension as given by Eq. (40), is reported in the third column of Table 1. The different methods described above to compute the surface tension provide predictions that are in a reasonably good agreement. In all cases, the surface tension diminishes when temperature increases and values for higher temperatures than those reported can be inferred by knowing that $\gamma \to 0$ at $T = T_c$. The Guggenheim-Katayama power law is a theoretically sound choice of function form for data fitting [21] of surface tension versus temperature and yields to the following regression

$$\gamma = a \left(1 - \frac{T}{T_c}\right)^b \tag{41}$$

As an application, the data fitting of the first column of Table 1 provides $a = 1.14835$ and $b = 1.41037$.

TABLE 1. Surface tension as a function of the dimensionless temperature T/T_c obtained by different methods. (A) Eq. (28) with p_{xx} as given by Eq.(29). (B) Eq. (28) with p_{xx} as given by Eq.(30). (C) Eq. (40)

	γ		
T/T_c	(A)	(B)	(C)
0.66	0.247	0.300	0.250
0.73	0.184	0.193	0.178
0.79	0.123	0.114	0.121
0.86	0.0698	0.0577	0.0675
0.93	0.0277	0.0199	0.0266

4.2. **Contact angle.** In capillary flows inside microchannels the interaction between the fluid and the wall plays a major role. Usually the fluid-wall interaction promotes inhomogeneity in the fluid and thus it affects the equilibrium and dynamic behavior of the fluid itself [18]. A parameter that macroscopically encompasses the fine details of fluid-wall interaction is the contact angle θ between the solid surface and the tangent to the liquid surface at contact with the solid [26]. In our model the fluid-solid interaction is characterized by the dimensionless parameters σ_g/σ_w, m_g/m_w, $\tilde{n}_w$, $\overline{\phi}_{gw}/k_BT_0$, γ_{gw}. The first two parameters are constant and assume the values written in Sec. 4 for all the results shown here. In this section we assess the effect of $\overline{\phi}_{gw}$, $\tilde{n}_w$, and γ_{gw} on the contact angle.

TABLE 2. Fluid wall interaction parameters for isolated drop.

	$\overline{\phi}_{gw}/k_BT_0$	γ_{gw}	$\tilde{n}_w\pi\sigma_{gw}^3/6$
A	1.0	0.185	0.7
B	1.5	0.185	0.7
C	1.5	0.185	0.57
D	1.5	0.022	0.57

An isolated fluid drop in contact with the lower wall, located at $y/\sigma_g = -11$, of a microchannel has been simulated for varying values of the above parameters as it is reported in Table 2. In these computations the upper microchannel wall, located at $y/\sigma_g = 13$, has been replaced by a specular reflective surface. At time $t = 0$ a

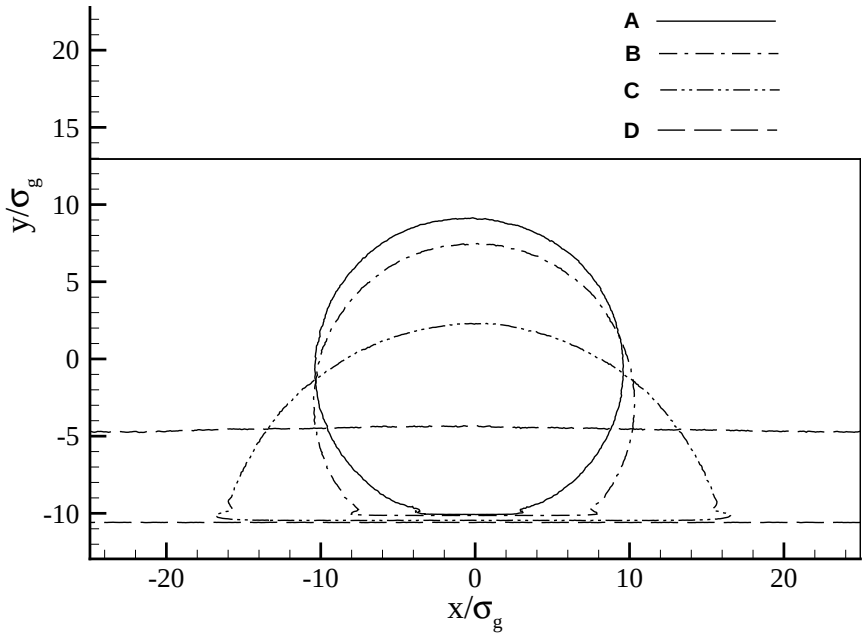

FIGURE 2. Contact angle of an isolated drop.

half spherical drop is placed in contact with the lower wall of the microchannel and this initial configuration evolves until a steady state is reached.

The outcome of the computations is shown in Fig. 2. Going from case A to case D the wall behavior changes from hydrophobic to hydrophilic, thus showing the capability of Enskog-Vlasov approach to simulate the full range of fluid-wall interaction behavior. The difference between case A and B is uniquely in the value of $\overline{\phi}_{gw}/k_BT_0$, the attractive tail of case B being stronger than the one of case A; however the wall is still hydrophobic. In case C the contact angle is less than $\pi/2$ and the wall is partially hydrophilic; with respect to case B we have changed the value of $\tilde{n}_w\pi\sigma_{gw}^3/6$ from 0.7 to 0.57. The net effect of decreasing $\tilde{n}_w$ is to reduce the strength of the hard-sphere repulsive part of the interaction potential. In case D the wall is totally hydrophilic, the initial drop has wetted the wall and the contact angle is practically zero. The value of $\tilde{n}_w$ is unchanged, but the value of γ_{gw} has been increased from 0.185 to 0.22 and this broadens the range of the attractive tail of the gas-wall potential. The transition from hydrophobic to hydrophilic behavior is clearly governed by the mutual balance of the attractive tail of gas-wall potential and of the hard-sphere repulsive core. This hydrophilic case D is of technological interest because the wall surface of many micro and nano electromechanical systems is silicon based and is therefore totally hydrophilic with respect to water. Such an observation justifies the choice of keeping $\overline{\phi}_{gw}/k_BT_0 = 1.5$, $\gamma_{gw} = 0.22$ and $\tilde{n}_w\pi\sigma_{gw}^3/6 = 0.57$ for all the remaining results.

4.3. **Laplace-Kelvin equation.** The capability of the kinetic model to deal with dense capillary flows is further supported by studying, in the two dimensional case, the structure of a meniscus between two hydrophilic walls set at a distance d from each other. At equilibrium the relation between the gas phase pressure, p, and the

meniscus mean curvature, K, is given by the Laplace-Kelvin equation

$$\ln\left(\frac{p}{p_s}\right) = \frac{\gamma V_l}{\mathcal{R}T} K \tag{42}$$

where V_l is the molar volume of the liquid phase, p_s is the saturation pressure of the gas phase when the interface between vapor and liquid is planar, $\mathcal{R}$ the universal gas constant, T the temperature, γ the surface tension of the liquid-vapor interface. The ratio p/p_s is usually called the relative humidity and denoted by RH. The mean curvature K is linked to the two principal radii of the meniscus surface through the relation $K = 1/R_1 + 1/R_2$. In the two dimensional case one of the two radii tends to infinity and therefore $K = d/2$ when the contact angle is equal to zero. The computations have been carried out for values of the distance d between the two walls in the range $[5\sigma_g, 25\sigma_g]$ and for two values of temperature, $T/T_0 = 0.5$ and $T/T_0 = 0.6$. At time $t = 0$ a vertical strip of liquid, surrounded by the gas phase, is placed in the middle of the microchannel. The strip spans the entire distance between the two walls and can have different initial widths. This initial configuration evolves in time until a steady state is reached. When the initial width is too narrow the strip separates into two parts that wet the upper and lower wall, otherwise a meniscus forms between the two walls. The system is thermostatted to keep the temperature constant during the transient phase. In Fig. 3 the solid circles are the computed values of RH versus the wall distance for an initial strip of width $16\sigma_g$ and temperature $T/T_0 = 0.5$, the solid squares are values of RH for an initial strip of width $16\sigma_g$ and temperature $T/T_0 = 0.6$. The solid and dashed lines are Eq. (42), computed with the relevant values of the surface tension that appear in the fourth column of Table 1.

The values of RH computed for $d \geq 8\sigma_g$ agree reasonably well with the values predicted by the Laplace-Kelvin equation, especially for $T/T_0 = 0.5$, whereas a non negligible discrepancy can be noticed for $d = 5\sigma_g$. However, it is worth noticing that for this value of the wall distance, the interaction with the wall dominates the flow and it is not possible any more to identify a bulk for the gas phase, a requirement on which Eq. (42) is based. This fact is shown in Fig. 4 that reports the reduced density $\eta_g = n_g \pi \sigma_g^3/6$ profile along a vertical section at abscissa $x/\sigma_g = -10$ from the middle of the channel, i.e. outside the portion of the channel occupied by the meniscus. In the left panel of Fig. 4 the channel wall is located at $|y/\sigma_g| = 2.5$ and in the right panel at $|y/\sigma_g| = 8$. In the right panel of Fig. 4, which refers to $d = 16\sigma_g$, the existence of the uniform gas phase bulk is evident for $|y/\sigma_g| < 3$, whereas in the left panel, which refers to $d = 5\sigma_g$, the gas phase bulk disappears and the Laplace-Kelvin formula does not fit any more the numerical results. We remark that the bulk of the gas phase is narrower for $T/T_0 = 0.6$ than for $T/T_0 = 0.5$, because the width of the interface between vapor phase and liquid phase increases with temperature. This explains why in Fig. 3 the agreement between the predictions of the Laplace-Kelvin equation and the numerical results is marginally better for $T/T_0 = 0.5$ than for $T/T_0 = 0.6$.

Inspecting Fig. 4 we notice that, outside the region occupied by the liquid meniscus, it exists a thin layer of liquid adsorbed over the channel wall, that becomes vapor sufficiently far from the wall. As the density profiles in Fig. 4 show, the liquid film strongly differs from a fully developed one, *i.e.* it does not show distinct bulk and interface regions with density values close to liquid-vapor coexistence curve. We remark that the interaction between the fluid and the wall substantially alters the

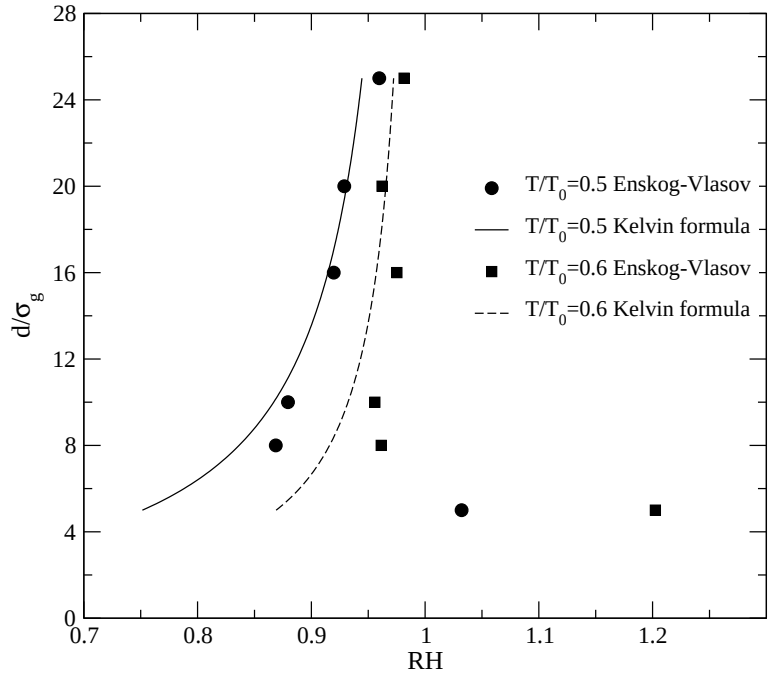

FIGURE 3. Relative humidity, $RH = p/p_s$, versus microchannel wall distance, d/σ_g. Solid circles and squares: numerical predictions of the Enskog-Vlasov equation, Eq. (11), for $T/T_0 = 0.5$ and $T/T_0 = 0.6$, respectively. Solid and dashed lines: predictions of the Kelvin-Laplace formula, Eq. (42), for $T/T_0 = 0.5$ and $T/T_0 = 0.6$, respectively.

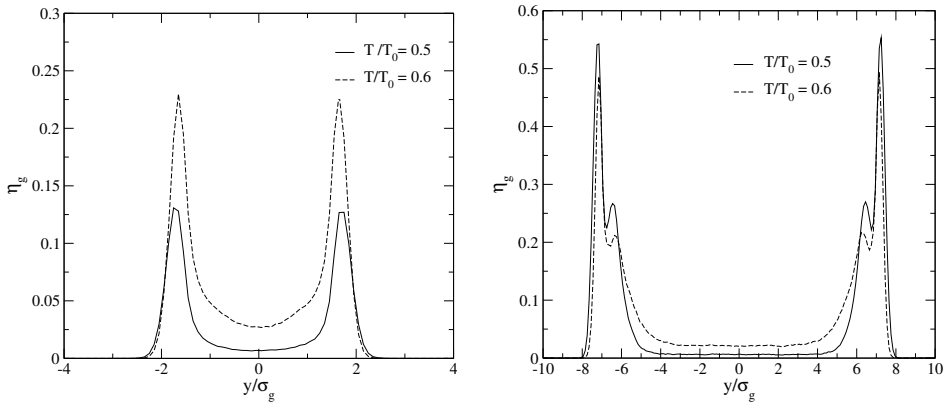

FIGURE 4. Reduced density plot at $x/\sigma_g = -10$. **Left** $d = 5\sigma_g$. **Right** $d = 16\sigma_g$.

structure of the liquid layer and of the interfacial region with respect to the planar interface without wall interaction. It is precisely this fact that makes possible to have at the same time a planar interface and $RH < 1$, at least for the case of an

hydrophilic wall. As a matter of fact, fully developed liquid films attached to each planar wall and a liquid meniscus of finite radius bridging them are not compatible since they would be in equilibrium with different values of the RH parameter.

As the distance between the solid walls is increased, the meniscus radius increases and the liquid film structure adjusts to match a higher RH value. The process can be seen in Fig. 5 showing the profile of reduced density η_g along a vertical section of the channel, far from the meniscus, for different values of the walls distance d. Only one of the two identical films is shown and the space coordinate has been shifted such that the wall is located at $y/\sigma_g = 0$ for all the computations. The solid line corresponds to $RH = 0.88$ and $d = 8\sigma_g$, the dashed lines to $RH = 0.96$ and $d = 25\sigma_g$, the dot-dashed line to $RH = 0.98$ and $d = 40\sigma_g$ and finally the dot-dashed-dashed line to the limit case of a planar fully developed interface with $RH = 1$ and $d \to \infty$.

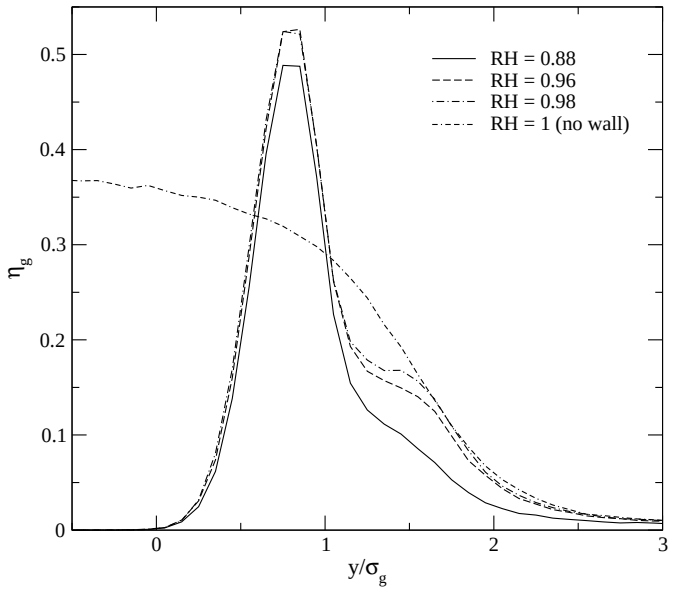

FIGURE 5. Reduced density profile at the wall for different wall distances.

4.4. **Conditions for the meniscus breakage.** Stability and breaking of liquid bridges and menisci is a widely investigated subject [9], on the ground of classical fluid mechanics. More recently, some aspects of nanosized liquid bridges have been investigated by MD simulation, showing that different breaking patterns are possible in response to different external conditions [22]. The results described in this section are far to represent a comprehensive study. The aim is only to show that the model has the capability to describe the dynamical unsteady process leading to meniscus formation and breakage. In Sec. 4.3, we have already shown the ability of the model to follow the formation of menisci in microchannels. The initial condition is indeed quite artificial, but nothing prevents to initialize the computations by more realistic configurations. Notice should be made that the breakage is expected not to be related to the Rayleigh-Plateau instability, namely the instability due to long-wave perturbations in the direction of homogeneity. As a matter of fact,

these perturbations are not accounted for in the z direction because of the two-dimensional nature of the problem. Furthermore, they can not even develop and grow in the y direction because of the relatively short distance between the solid walls that confine liquid menisci.

Meniscus breakage is studied as follows. Simulation starts with a stable meniscus and a strip of particles is removed from its central zone, thus effectively reducing its width and introducing also an initial perturbation. The newly formed meniscus is then evolved in time until either a stable configuration is reached or the meniscus breaks down. The procedure has been applied to the meniscus formed by an initial strip of width $16\sigma_g$ between two walls set at a distance $d = 25\sigma_g, 20\sigma_g$ and $d = 16\sigma_g$ from each other. In all the computations T/T_0 has been set equal to 0.5. Fig. 6 shows, for the case $d = 25\sigma_g$, the reduced density η_g across the horizontal channel section placed at $y/\sigma_g = 0$, which corresponds to the meniscus throat. The solid line (meniscus 1) refers to the stable meniscus formed by an initial strip of width $16\sigma_g$, the dashed line (meniscus 2) to the stable meniscus formed after removing a strip of width $4\sigma_g$ from the center of meniscus 1. The dashed-dotted line (meniscus 3) corresponds to the stable meniscus formed after removing a strip of width $2\sigma_g$ from meniscus 2. The doubled dashed-dotted line (meniscus 4) corresponds to the meniscus obtained by removing again a strip of width $2\sigma_g$ from the center of meniscus 3. This final configuration is unstable and breaks down at the throat; its reduced density profile is extracted from an average over a time interval $\Delta t = 25\frac{\sigma_g}{RT_0}$, before the meniscus starts to break. The contour plots of the reduced density immediately before and after the meniscus breakage are shown in Fig. 7 for the case $d = 25\sigma_g$; they correspond to the unstable configuration meniscus 4 of Fig. 6. The computations performed for $d = 20\sigma_g$ and $d = 16\sigma_g$ follow a perfectly analogous trend. The shape of breaking meniscus depicted in Fig. 7 strongly resembles the double cone configuration [22] which seems to occur when the vapor pressure is very low, as in the case considered here. The density profiles in Fig. 7 and the coarse stability analysis presented above, indicate that a meniscus will not break as long as the interfaces on its two opposite sides keep their separation. Two competing mechanisms act at the meniscus throat. The fluid-fluid force field, $\mathbf{F}_{gg}(\mathbf{r}|t)$, due to the density gradient over the transition zone between the gas phase and the liquid phase, tends to squeeze the meniscus, i.e. is directed from the vapor to the liquid. Fig. 6 shows that, for a stable meniscus, the density profile in the transition region does not depend on the throat width and therefore the fluid-fluid force field is unchanged when the meniscus shrinks. On the opposite, the hard-sphere collisions, being repulsive, tend to expand the meniscus and counteract the force field $\mathbf{F}_{gg}(\mathbf{r}|t)$. However the force field generated by the collisions is not invariant with respect to the throat width. Collisions in a dense hard-sphere fluid are non-local and involve pairs of particles set at a distance σ_g one from the other, as shown in Eq. (8). A fluid particle that sits in the liquid phase close to the transition region will collide with particles that belong to the liquid zone and to the interface zone. Because density is higher in the liquid than in the interface, this particle will be more likely to collide with partners located in the liquid region. The net effect of collisions is therefore to generate a force directed from the liquid to the vapor, *i.e.* opposite to the force field $\mathbf{F}_{gg}(\mathbf{r}|t)$. The meniscus is stable at the throat until the two competing forces are able to balance each other. When the width of the liquid phase in the throat drops below a critical value, which from our computations seems to be around $2\sigma_g$ and seems also not to depend from wall distance, a local density

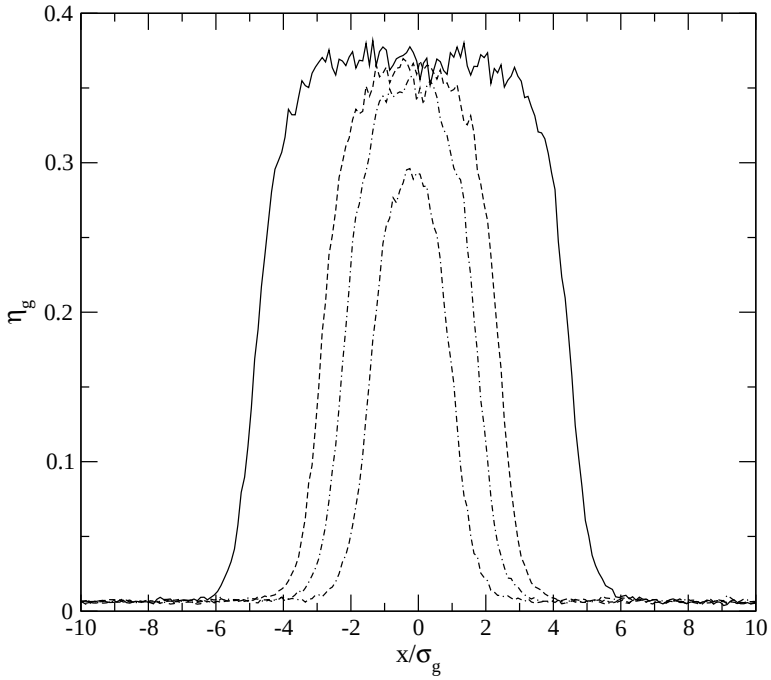

FIGURE 6. Reduced density plot at $y/\sigma_g = 0$, $d = 25\sigma_g$.

fluctuation lowering the density in the remaining thin liquid layer can effectively reduce the collision rate and the repulsive effect of the hard sphere potential in the whole throat thickness, thus leading to the merging of the opposite interfaces and to meniscus collapse. It is worth observing that the perturbations and fluctuations leading to breaking have different origins in the performed simulations. Pressure and density perturbations in an initially static meniscus are artificially produced by particles removal. Spontaneous fluctuations are also present because of the particles representation of the distribution function. However, their intensity is related to the number of *simulation* particles which, as observed above, is not related to the number of real physical atoms in the system. Further analysis is required to assess the impact of simulations setup on the menisci stability analysis.

5. **Conclusions.** In the present work, a kinetic model for the study of unsteady capillary flows between solid walls has been presented. The model is based on the Enskog-Vlasov kinetic equation and provides a reasonable description of two-phase flows and of fluid-surface interaction, automatically tracking the formation of vapor-liquid and solid-liquid interfaces. In the latter case it is possible to simulate the full range of contact angles between the liquid and the solid, from hydrophobic surfaces to hydrophilic ones. Moreover, it can be solved with a modified DSMC technique with a computational cost that is substantially smaller than the corresponding molecular dynamic simulations. The structure of a stable meniscus bridging two hydrophilic walls has been studied and the validity range of the Laplace-Kelvin equation has been estimated. Meniscus breakage has been simulated and a possible explanation of the phenomenon has been given.

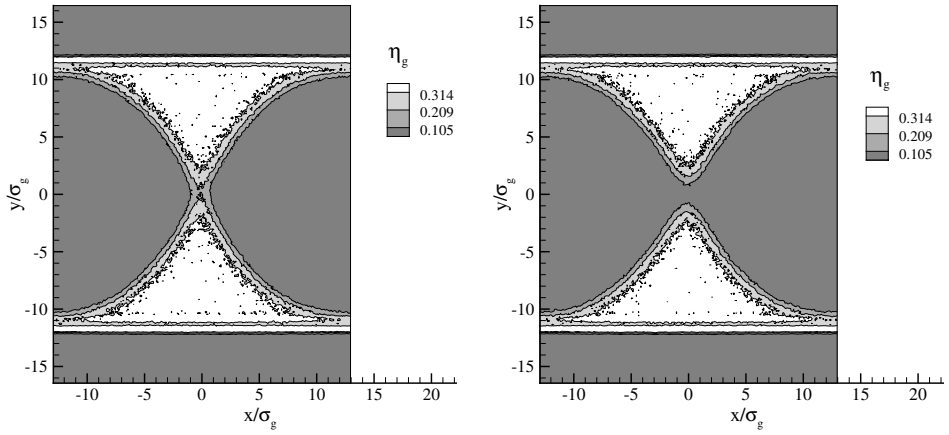

FIGURE 7. Unsteady simulation of meniscus breakage. Density contour plots for a meniscus immediately before (**Left**) and after (**Right**) its breakage. $d = 25\sigma_g$.

A number of future developments can be envisaged. A more detailed analysis of the stiction of MEMS surfaces due to capillary forces is certainly of interest. By means of the particle method of solution used in the present work, the adhesion force can be easily computed by directly evaluating the change of momentum of the gas molecules due to their interaction with wall molecules. This interaction includes both short-range hard-sphere collisions and the long-range mean force field. A second aspect worth to be investigated is the dynamics of liquid menisci between moving walls in order to provide a more realistic model of capillary flows in micromechanical devices and, in particular, to provide an assessment of the validity of the present quasi-static approach when applied to devices having moving parts at high frequency.

REFERENCES

[1] M. Allen and D. Tildesley, *Computer Simulation of Liquids*, Clarendon Press, 1989.
[2] R. Ardito, A. Corigliano and A. Frangi, Multiscale finite element models for predicting spontaneous adhesion in MEMS, *Mecanique Industries*, **11** (2010), 177–182.
[3] P. Barbante, A. Frezzotti, L. Gibelli and D. Giordano, A kinetic model for collisional effects in dense adsorbed gas layers, in *Proceedings of the 27th International Symposium on Rarefied Gas Dynamics* (eds. I. Wysong and A. Garcia), vol. 1333 of AIP Conference Proceedings, 2010, 458–463.
[4] P. Barbante, A. Frezzotti, L. Gibelli, P. Legrenzi, A. Corigliano and A. Frangi, A kinetic model for capillary flows in MEMS, in *Proceedings of the 28th International Symposium on Rarefied Gas Dynamics* (eds. M. Mareschal and A. Santos), vol. 1501 of AIP Conference Proceedings, 2012, 713–719.
[5] G. Bird, *Molecular Gas Dynamics and the Direct Simulation of Gas Flows*, Clarendon Press, Oxford, 1994.
[6] N. Carnahan and K. Starling, Equation of state for nonattracting rigid spheres, *J. Chem. Phys.*, **51** (1969), 635–636.
[7] C. Cercignani, *The Boltzmann Equation and Its Applications*, Springer, Berlin, 1988.
[8] S. Cheng and M. Robbins, Capillary adhesion at the nanometer scale, *Phys. Rev. E*, **89**, (2014), 062402.
[9] J. Eggers, Nonlinear dynamics and breakup of free-surface flows, *Reviews of Modern Physics*, **69** (1997), 865–929.

[10] D. Enskog, Kinetische theorie der wärmeleitung, reibung und selbstdiffusion in gewissen verdichteten gasen und flüssigkeiten, *K. Svensk. Vet. Akad. Handl.*, **63** (1922), 5–44.
[11] J. Fischer and M. Methfessel, Born-Green-Yvon approach to the local densities of a fluid at interfaces, *Phys. Rev. A*, **22** (1980), 2836–2843.
[12] A. Frezzotti, A particle scheme for the numerical solution of the Enskog equation, *Phys. Fluids*, **9** (1997), 1329–1335.
[13] A. Frezzotti and L. Gibelli, A kinetic model for equilibrium and non-equilibrium structure of the vapor-liquid interface, in *Proceedings of the 23rd International Symposium on Rarefied Gas Dynamics* (eds. A. Ketsdever and E. Muntz), vol. 663 of AIP Conference Proceedings, 2003, 980–987.
[14] A. Frezzotti and L. Gibelli, A kinetic model for fluid wall interaction, *Proc. IMechE, Part C: J. Mech. Eng. Science*, **222** (2008), 787–795.
[15] A. Frezzotti, L. Gibelli and S. Lorenzani, Mean field kinetic theory description of evaporation of a fluid into vacuum, *Phys. Fluids*, **17** (2005), 012102.
[16] A. Frezzotti, S. Nedea, A. Markvoort, P. Spijker and L. Gibelli, Comparison of molecular dynamics and kinetic modeling of gas-surface interaction, in *Proceedings of the 26th International Symposium on Rarefied Gas Dynamics* (ed. T. Abe), vol. 1084 of AIP Conference Proceedings, 2009, 635–640.
[17] M. Grmela, Kinetic equation approach to phase transitions, *J. Stat. Phys.*, **3** (1971), 347–364.
[18] Z. Guo, T. Zhao and Y. Shi, Simple kinetic model for fluid flows in the nanometer scale, *Phys. Rev. E*, **71** (2005), 035301(R).
[19] J. Hansen and I. McDonald, *Theory of Simple Liquids*, Academic Press, 2006.
[20] A. Hariri, J. Zu, J. Zu and R. B. Mrad, Modeling of wet stiction in microelectromechanical systems MEMS, *J. Microelectromech. Syst.*, **16** (2007), 1276–1285.
[21] J. Hirschfelder, C. Curtiss and R. Bird, *The Molecular Theory of Gases and Liquids*, Wiley-Interscience, 1964.
[22] W. Kang and U. Landman, Universality crossover of the pinch-off shape profiles of collapsing liquid nanobridges in vacuum and gaseous environments, *Physical Review Letters*, **98** (2007), 064504.
[23] J. Karkheck and G. Stell, Mean field kinetic theories, *J. Chem. Phys.*, **75** (1981), 1475–1487.
[24] G. Karniadakis, A. Beskok and A. Narayan, *Microflows and nanoflows: Fundamentals and simulation*, Springer, Berlin, 2005.
[25] R. Maboudian and R. Howe, Critical review: stiction in surface micromechanical structures, *J. Vac. Sci. Technol. B*, **15** (1997), 1–19.
[26] J. Rowlinson and B. Widom, *Molecular theory of capillarity*, Dover Pubns, 2003.
[27] H. van Beijeren and M. Ernst, The modified Enskog equation, *Physica*, **68** (1973), 437–456.

E-mail address: paolo.barbante@polimi.it
E-mail address: aldo.frezzotti@polimi.it
E-mail address: livio.gibelli@polimi.it